CARDIOMYOPATHY

Epicardial differentiation drives fibro-fatty remodeling in arrhythmogenic cardiomyopathy

Arwa Kohela[1], Sebastiaan J. van Kampen[1], Tara Moens[1], Martijn Wehrens[1], Bas Molenaar[1], Cornelis J. Boogerd[1], Jantine Monshouwer-Kloots[1], Ilaria Perini[1], Marie José Goumans[2], Anke M. Smits[2], J. Peter van Tintelen[3], Eva van Rooij[1,4]*

Arrhythmogenic cardiomyopathy (ACM) is an inherited disorder often caused by pathogenic variants in desmosomal genes and characterized by progressive fibrotic and fat tissue accumulation in the heart. The cellular origin and responsible molecular mechanisms of fibro-fatty deposits have been a matter of debate, due to limitations in animal models recapitulating this phenotype. Here, we used human-induced pluripotent stem cell (hiPSC)–derived cardiac cultures, single-cell RNA sequencing (scRNA-seq), and explanted human ACM hearts to study the epicardial contribution to fibro-fatty remodeling in ACM. hiPSC-epicardial cells generated from patients with ACM showed spontaneous fibro-fatty cellular differentiation that was absent in isogenic controls. This was further corroborated upon siRNA-mediated targeting of desmosomal genes in hiPSC-epicardial cells generated from healthy donors. scRNA-seq analysis identified the transcription factor TFAP2A (activating enhancer-binding protein 2 alpha) as a key trigger promoting this process. Gain- and loss-of-function studies on hiPSC-epicardial cells and primary adult epicardial-derived cells demonstrated that TFAP2A mediated epicardial differentiation through enhancing epithelial-to-mesenchymal transition (EMT). Furthermore, examination of explanted hearts from patients with ACM revealed epicardial activation and expression of TFAP2A in the subepicardial mesenchyme. These data suggest that TFAP2A-mediated epicardial EMT underlies fibro-fatty remodeling in ACM, a process amenable to therapeutic intervention.

INTRODUCTION

Arrhythmogenic cardiomyopathy (ACM) is a hereditary disease characterized by ventricular arrhythmias and progressive ventricular remodeling that may ultimately lead to heart failure (*1*). The predominant cause of ACM is the presence of pathogenic variants in genes encoding proteins that form the desmosome, a multiprotein complex connecting adjacent cardiac cells (*2*). A characteristic feature of ACM is the progressive replacement of the myocardium with fibrotic and fat tissue, which further promotes ventricular dysfunction (*3*, *4*). To study ACM disease mechanisms, many ACM animal models have been developed that have helped understand the electrical instabilities seen in patients [reviewed in (*5*, *6*)]. However, studying the fibro-fatty phenotype has been challenging, because most experimental animal models do not naturally develop the cardiac adipose tissue seen in humans (*7*). Thus, to better understand ACM pathophysiology, human models of ACM are required.

The epicardium is the outer mesothelial layer of the heart that acts as a multipotent progenitor cell population and a source of paracrine factors that signal to the myocardium (*8*, *9*). During embryonic development, the epicardium undergoes epithelial-to-mesenchymal transition (EMT), giving rise to epicardial-derived cells (EPDCs) that can differentiate into smooth muscle cells and fibroblasts. This process contributes to myocardial growth and vascularization (*10*). In the postnatal heart, the epicardium is mainly quiescent and forms a single membranous layer covering the myocardium. However, cardiac injury or stress can induce epicardial activation, proliferation, and EMT, giving rise to various cardiac cell types that can migrate to and repopulate the myocardium (*8*, *9*, *11*–*13*). Given the multipotent potential of epicardial cells during both cardiac development and disease, we examined whether they contribute to the pathological fibro-fatty remodeling in ACM.

Here, we showed that human-induced pluripotent stem cell (hiPSC)–derived epicardial cells from patients with ACM harboring mutations in the desmosomal gene plakophilin-2 (*PKP2*) spontaneously differentiated into fibroblasts and fat cells. This effect appeared to be due to desmosomal disruption, because we observed similar effects after desmosomal inhibition in control hiPSC-epicardial cells. We identified transcription factor activating enhancer-binding protein 2 alpha (TFAP2A) as a key transcription factor driving this process in diseased epicardial cells. Knockdown of *TFAP2A* reduced fibro-fatty gene expression in mutant epicardial cells as well as in control and primary adult epicardial cultures undergoing EMT. Examining explanted heart tissue from patients with ACM revealed epicardial thickening, activation through wilms tumor 1 (WT1) expression, and TFAP2A induction in the subepicardial mesenchyme. These findings suggest that TFAP2A-mediated epicardial–to–fibro-fatty cellular transition upon desmosomal disruption is an important underlying cause for the fibro-fatty replacement observed in ACM.

RESULTS

Epicardial cultures can be generated from PKP2-corrected and c.2013delC hiPSCs

Pathogenic variants in the five major genes encoding desmosomal proteins can be identified in about 60% of patients with ACM, most commonly in *PKP2* (up to 46% of all patients). However, nondesmosomal pathogenic variants have also been linked to ACM (Fig. 1A) (*2*, *14*). On the basis of the multipotent potential of epicardial cells

[1]Hubrecht Institute, Royal Netherlands Academy of Arts and Sciences (KNAW), 3584 CT Utrecht, Netherlands. [2]Department of Cell and Chemical Biology, Leiden University Medical Center, 2300 RC Leiden, Netherlands. [3]Department of Genetics, University Medical Centre Utrecht, 3584 CX Utrecht, Netherlands. [4]Department of Cardiology, University Medical Centre Utrecht, 3584 CX Utrecht, Netherlands.
*Corresponding author. Email: e.vanrooij@hubrecht.eu

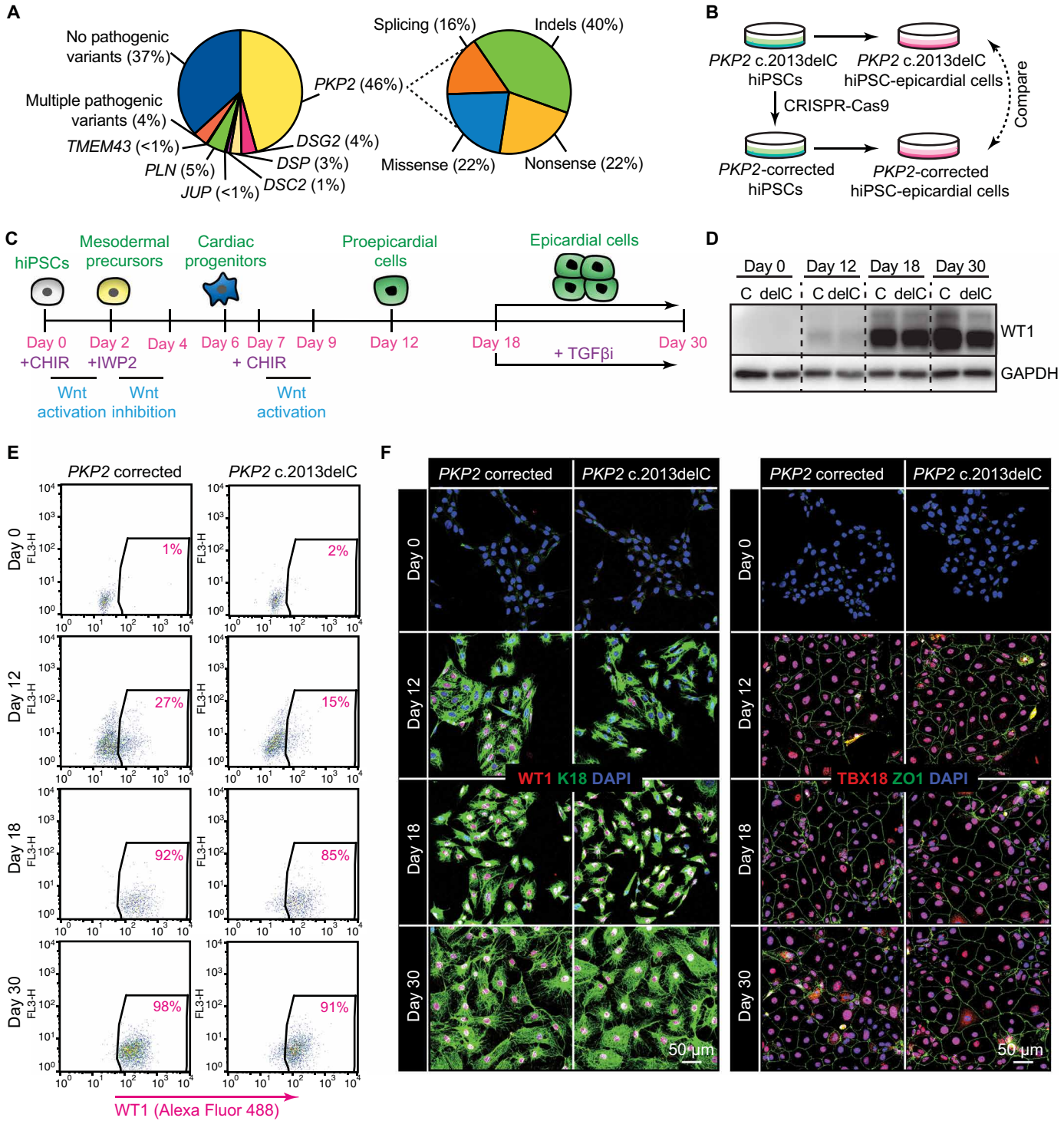

Fig. 1. Generation of epicardial cells from *PKP2*-corrected and c.2013delC hiPSCs. (**A**) Pie charts showing the distribution of genes underlying ACM (left) and reported pathogenic *PKP2* variants (right). (**B** and **C**) Schematics of hiPSC to epicardial cell differentiation protocol. (**D** and **E**) Representative analysis of WT1 expression by (D) Western blot and (E) flow cytometry in *PKP2*-corrected and c.2013delC hiPSC-epicardial cells at different culture time points. (**F**) Immunofluorescence staining for the indicated epicardial markers in *PKP2*-corrected and c.2013delC hiPSC-epicardial cells. C, *PKP2* corrected; delC, *PKP2* c.2013delC. Data in (D) to (F) are representative of three independent experiments.

and the subepicardial predominance of the fibro-fatty deposits (*15*), we studied the effect of desmosomal gene mutations in epicardial cells. To this end, we used hiPSCs from a patient with ACM carrying a pathogenic *PKP2* mutation (*PKP2* c.2013delC) and generated its isogenic control (*PKP2* corrected) using CRISPR-Cas9 (fig. S1, A to C). The corrected line showed a normal karyotype, pluripotency

status, and no sequence defects in the top predicted off-target sites (fig. S1, D to F).

PKP2-corrected and c.2013delC hiPSCs were differentiated into epicardial cells (hiPSC-epicardial cells) using an adapted and optimized protocol from Bao *et al.* (*16*) (Fig. 1, B and C). This differentiation protocol relies on the generation of cardiac progenitors by day 6 of differentiation using small-molecule Wnt pathway modulators. Subsequent to this stage, cells would spontaneously differentiate into beating cardiomyocytes. However, reactivation of Wnt signaling induces an epicardial cell fate (fig. S2, A to C). Epicardial differentiation was confirmed by the time-dependent increased expression in the epicardial markers WT1, K18, TBX18, and ZO1 (*16*), reaching a highly pure epicardial cell population (>90%) after 1 month of differentiation (Fig. 1, D to F, and fig. S3). The localization of the desmosomal proteins PKP2, plakoglobin (PKG), desmoplakin (DSP), desmoglein-2 (DSG2) and desmocollin-2 (DSC2) did not appear to be altered in the diseased epicardial cells (fig. S4).

PKP2 c.2013delC hiPSC-epicardial cells display enhanced fibro-fatty signaling

To assess the molecular differences between *PKP2*-corrected and c.2013delC hiPSC-epicardial cells, we subjected both lines to RNA sequencing (RNA-seq). Compared to corrected controls, we observed a significant 50% reduction in wild-type *PKP2* expression in c.2013delC hiPSC-epicardial cells (fig. S5, A to C; $P < 0.05$). In addition, few mutant *PKP2* transcripts could be detected, indicating haploinsufficiency as a likely cause of the disease (fig. S5D).

When comparing global gene expression changes, we identified 125 down-regulated [$\log_2$ fold change (FC) < −2] and 472 up-regulated ($\log_2$FC > 2) genes (Fig. 2A and fig. S6; $P < 0.05$). Gene ontology (GO) analysis showed that up-regulated genes were involved in differentiation processes and adipogenesis and down-regulated genes were involved in collagen degradation (Fig. 2B). Key regulators of adipogenesis (*PPARG*, *PPARGC1A*, *UCP1*, *RORA*, and *CEBPA*) and fibroblast activation (*POSTN*, *FN1*, *COL1A2*, and *COL2A1*) were significantly induced in *PKP2* c.2013delC hiPSC-epicardial cells compared to the *PKP2*-corrected cells (Fig. 2C; $P < 0.001$), despite the comparable epicardial fate of cells at 1 month of differentiation, which led us to extend our cultures. At day 80 of differentiation, *PKP2* c.2013delC hiPSC-epicardial cells, and not their corrected counterparts, showed a marked loss of the expression of the epicardial marker WT1 (Fig. 2, D to F) and a significant induction in fat and fibrosis markers (fig. S7; $P < 0.05$), indicating a spontaneous cell fate transition in the diseased epicardial cells. In addition, only *PKP2* c.2013delC hiPSC-epicardial cells showed significant accumulation of lipid droplets as revealed by Oil red O staining without any lipogenic stimuli (Fig. 2, G and H; $P < 0.0001$). These data indicate that the *PKP2* c.2013delC mutation activates a fibro-fatty transition that is specific for mutant epicardial cells.

TFAP2A is up-regulated during epicardial–to–fibro-fatty cell transition

To gain more insights into the cellular identities in *PKP2*-corrected and c.2013delC hiPSC-epicardial cells, we subjected long-term cultures to single-cell RNA-seq (scRNA-seq) (Fig. 3, A and B). In comparing cellular heterogeneity of our *PKP2*-corrected epicardial cell cultures and hiPSC-derived cultures published in other studies [endothelial cells (*17*) and cardiomyocytes (*18*)], we observed relatively little transcriptomic differences between epicardial cells (*WT1* 90%), whereas differentiation was less efficient for the other cultures [endothelial cells, *FLT1* 7% (*17*) and cardiomyocytes, *TNNT2* 35% (*18*)] (fig. S8). The efficiency of generating highly pure epicardial cell populations further supported the use of our cultures to study cellular differentiation processes that take place solely due to *PKP2* mutations.

To study the process of fibro-fatty differentiation, we next compared *PKP2*-corrected and c.2013delC hiPSC-epicardial cells and identified five distinct cellular clusters (Fig. 3C). Cells from cluster 1 originated from both *PKP2*-corrected and c.2013delC hiPSC-epicardial cells, whereas the other clusters were constituted from either mutant (clusters 2 and 5) or corrected cells (clusters 3 and 4) (Fig. 3, C and D). Clusters 1, 2, and 5 showed increased expression of fibroblast and adipogenic markers, whereas epicardial markers were decreased, further validating an epicardial–to–fibro-fatty switch in the mutant cells (Fig. 3E). Analysis of only *PKP2* c.2013delC hiPSC-epicardial cells showed that epicardial differentiation resulted in a mixed population of cells expressing either fibroblast or fat cell markers, indicating two possible transition fates (fig. S9). To assess the cellular events possibly triggering these transitions, we performed a pseudotime analysis (Fig. 3, F and G) and identified transcription factors differentially expressed between the branches (Fig. 3H and fig. S10). Transcription factor *TFAP2A* showed a clear induction in the mutant clusters (Figs. 2B and 3, H and I). Furthermore, using HOMER (Hypergeometric Optimization of Motif EnRichment), we identified a significant enrichment for TFAP2A binding motifs in promoters of genes differentially expressed in cluster 5, which only contains mutant cells, suggesting a potential role in driving fibro-fatty gene programs (Fig. 3J and fig. S11; $P < 0.001$).

TFAP2A mediates fibro-fatty transition in PKP2 c.2013delC hiPSC-epicardial cells in an EMT-dependent manner

The TFAP2 family of transcription factors comprises five members: TFAP2A, TFAP2B, TFAP2C, TFAP2D, and TFAP2E, among which TFAP2A and TFAP2C have been previously implicated in regulating EMT (*19*), lipid droplet biogenesis (*20*, *21*), and fibrosis (*22*), further suggesting their potential in mediating the phenotype of mutant epicardial cells.

During culture, *TFAP2A* expression progressively increased in *PKP2* c.2013delC hiPSC-epicardial cells compared to their corrected counterparts ($P < 0.01$; Fig. 4, A to C, and fig. S12A). To investigate whether TFAP2A is required for fibro-fatty gene signaling, we knocked down *TFAP2A* using small interfering RNAs (siRNAs) in *PKP2* c.2013delC hiPSC-epicardial cells at day 80 of culture (Fig. 4C and fig. S12A). Two days after transfection, we observed a reduction in the expression of several fibroblast and fat markers (Fig. 4D). Furthermore, *TFAP2A* overexpression in 1-month-old control hiPSC-epicardial cells generated from healthy donors induced the expression of fibro-fatty markers 3 days after transduction (Fig. 4, E to G, and fig. S12B). This was associated with reduced $WT1^+$ and increased α-smooth muscle $actin^+$ ($\alpha\text{-SMA}^+$) cells and lipid droplet accumulation (Fig. 4, H to J), providing further evidence that TFAP2A is a key mediator of fibro-fatty signaling in epicardial cells.

Epicardial cells reside in an epithelial state that upon activation can undergo EMT and start cellular differentiation (*8*, *9*). Therefore, we postulated that desmosomal disruption might act as an EMT-driving trigger. Using flow cytometry, we measured the expression of the mesenchymal markers CD73 and CD29 and observed similar expression at 1 month of differentiation in *PKP2*-corrected and

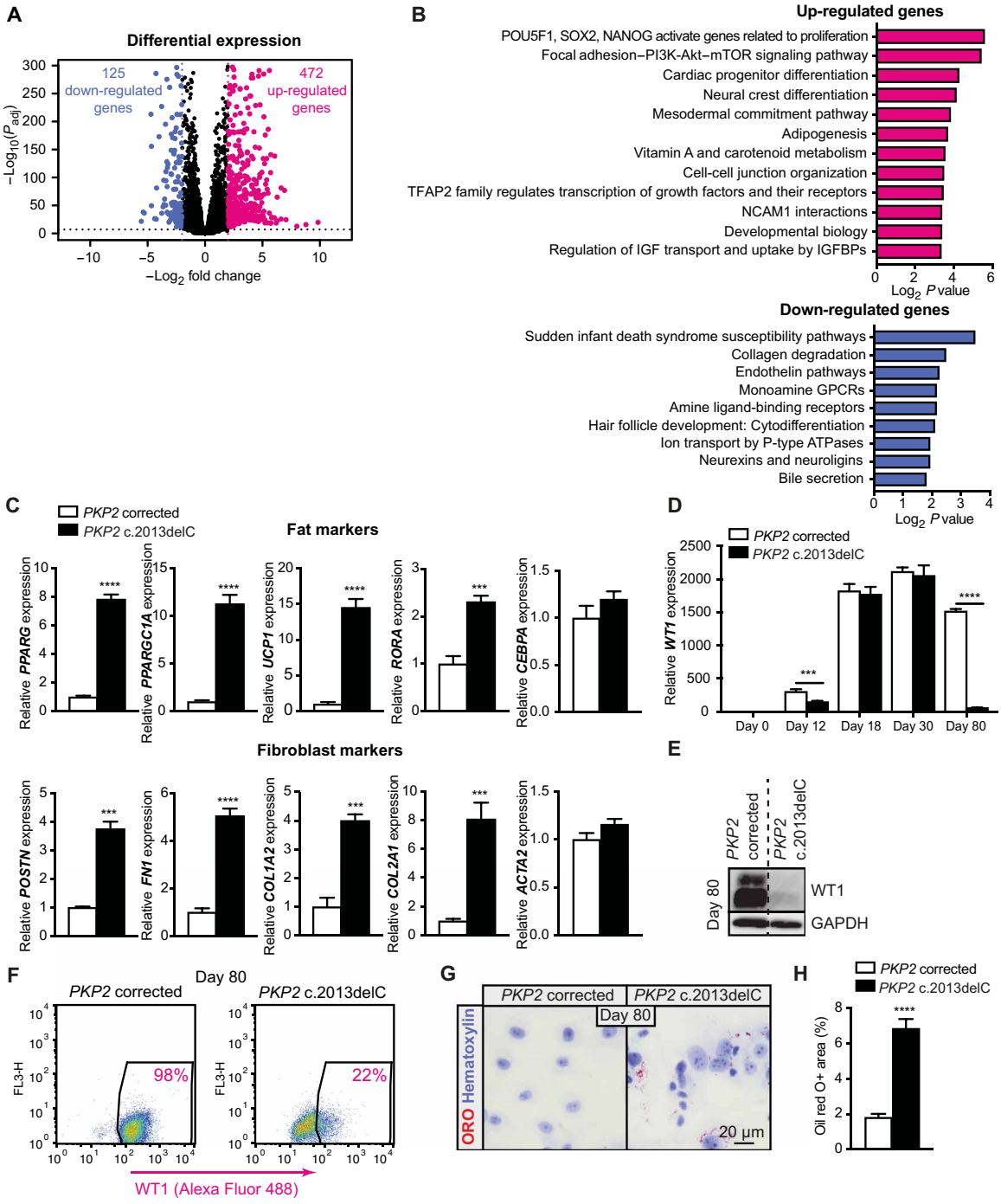

Fig. 2. Fibro-fatty gene signaling is induced in *PKP2* c.2013delC hiPSC-epicardial cells. (**A**) Volcano plot of differentially expressed genes identified by RNA-seq in 1-month-old *PKP2* c.2013delC versus corrected hiPSC-epicardial cells ($n = 4$). (**B**) ClueGO gene enrichment pathway analysis of differentially regulated genes identified by RNA-seq. (**C**) qPCR analysis of the indicated fat and fibroblast markers in 1-month-old *PKP2*-corrected and c.2013delC hiPSC-epicardial cells ($n = 4$). (**D**) Analysis of WT1 expression by qPCR during the culture timeline. Data represented as relative FC to day 0 *PKP2*-corrected cells ($n = 3$ to 4). (**E** and **F**) Representative analysis of WT1 expression on (E) Western blot and (F) flow cytometry in day 80 *PKP2*-corrected and c.2013delC hiPSC-epicardial cells. (**G**) Representative bright-field images of Oil red O (ORO) (lipid droplets) and hematoxylin-stained (nuclei) day 80 *PKP2*-corrected and c.2013delC hiPSC-epicardial cells. (**H**) Quantification of the Oil red O staining in (G). Data represented as relative FC to *PKP2*-corrected cells ($n = 10$). All data are means ± SEM. Statistical comparisons were evaluated using Student's *t* test (***$P < 0.001$; ****$P < 0.0001$).

c.2013delC hiPSC-epicardial cells. However, after 2 months of culture, expression of CD73 and CD29 was significantly induced in mutant cells, indicating an EMT switch preceding the fibro-fatty phenotype (Fig. 4K; $P < 0.05$). We also analyzed E-cadherin versus N-cadherin expression ratio (*CDH1/CDH2*), a measure of the epithelial versus mesenchymal state of the cells, and observed a

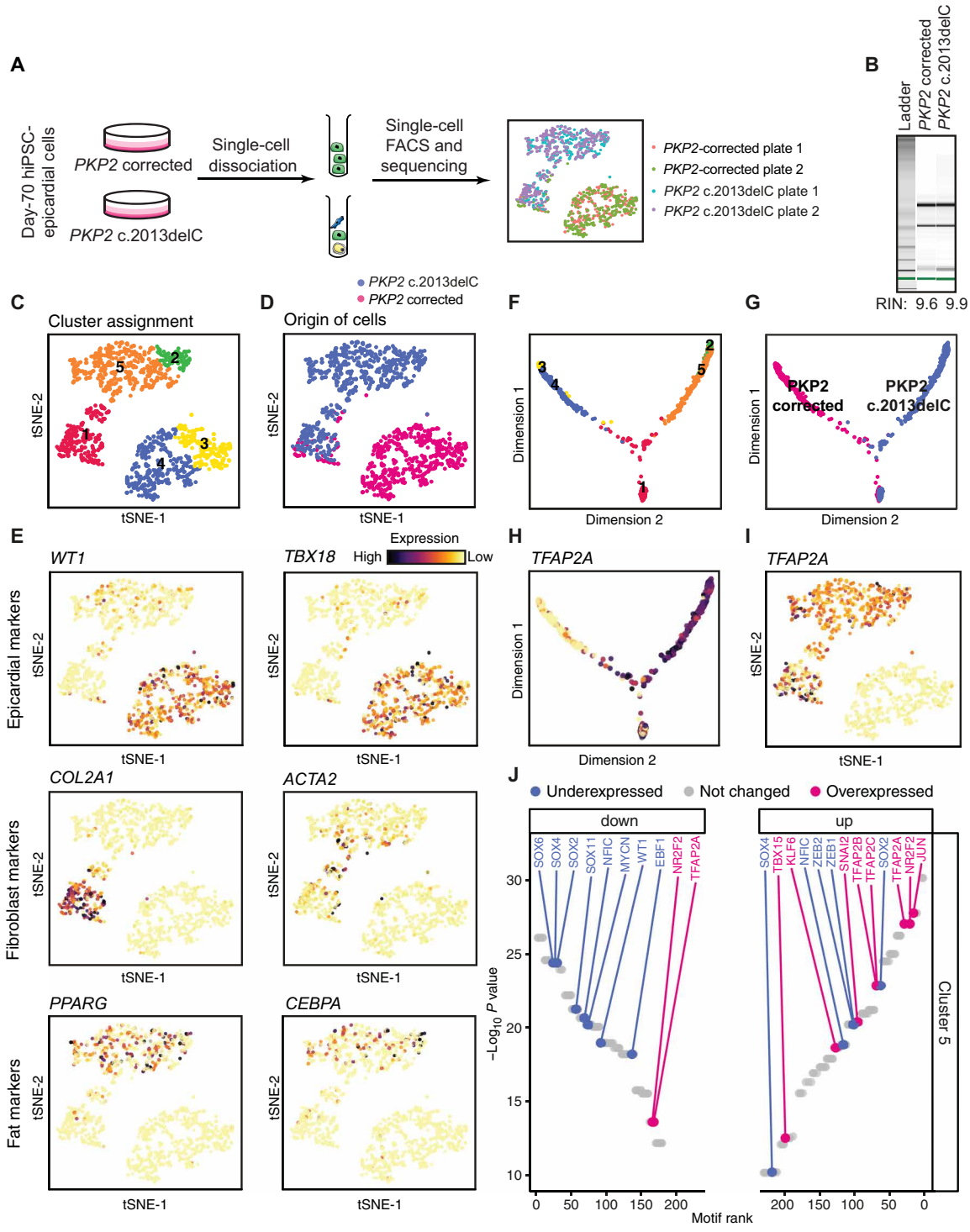

Fig. 3. scRNA-seq reveals *TFAP2A*-expressing clusters in *PKP2* c.2013delC hiPSC-epicardial cells. (**A**) Schematic of the scRNA-seq protocol. Day 70 *PKP2*-corrected and c.2013delC hiPSC-epicardial cells were dissociated and sorted into single cells for subsequent sequencing and in silico analysis ($n = 2$). FACS, fluorescence-activated cell sorting. (**B**) Representative bioanalyzer plots of sorted cells showing intact RNA indicated by RIN (RNA integrity number) values. (**C** and **D**) t-SNE maps of scRNA-seq analysis displaying (C) five distinct cellular clusters and (D) the origin of each cluster ($n = 2$). (**E**) t-SNE maps showing expression of different epicardial, fibroblast, and fat markers among cellular clusters ($n = 2$). (**F** and **G**) Pseudotime analysis of the different cellular clusters ($n = 2$). (**H** and **I**) *TFAP2A* expression presented in (H) pseudotime and (I) t-SNE plot ($n = 2$). (**J**) HOMER analysis of enriched transcription factor binding motifs in down-regulated (left) and up-regulated (right) genes identified in cluster 5 ($n = 2$). Color codes indicate whether transcription factors show differential gene expression.

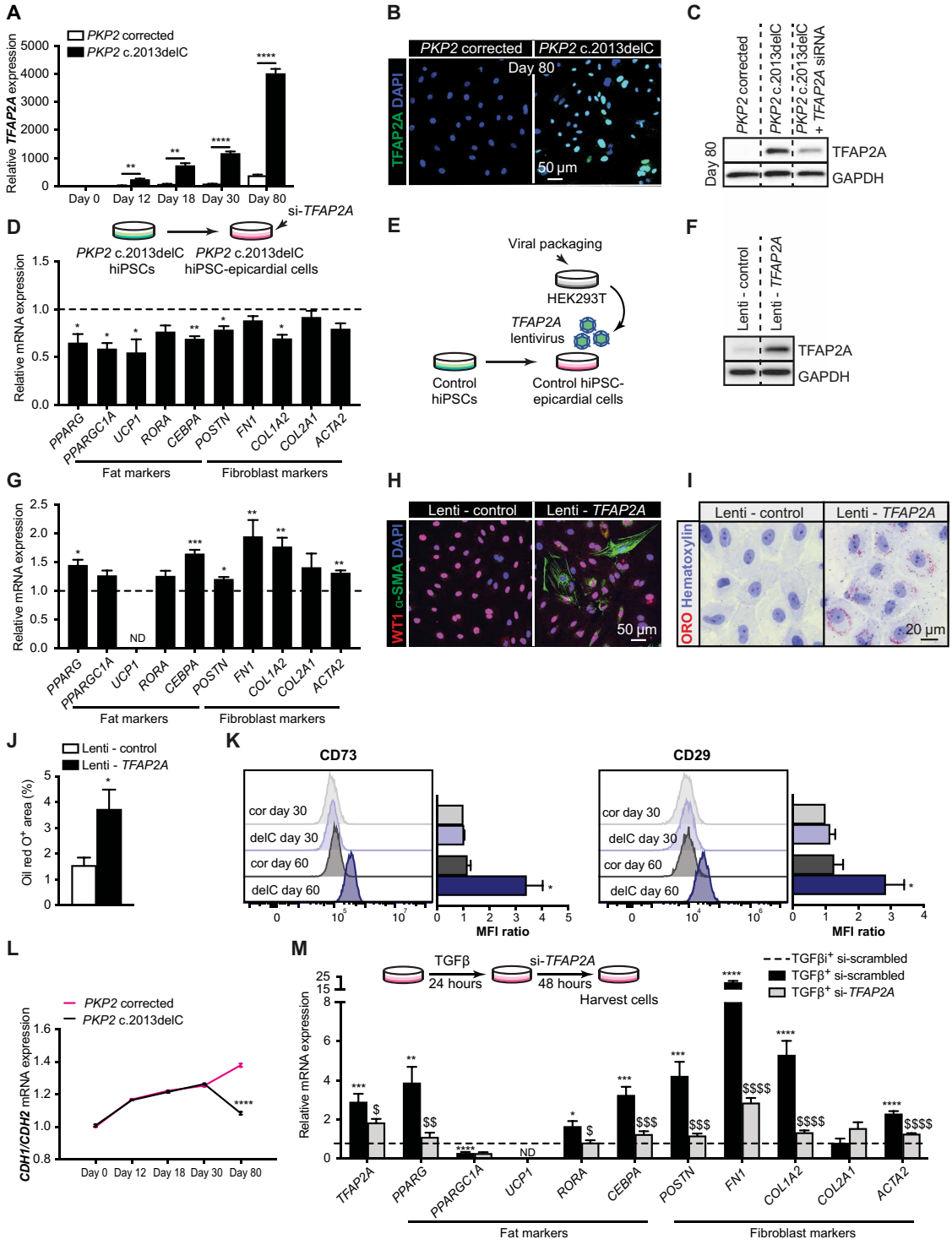

Fig. 4. TFAP2A mediates EMT and fibro-fatty signaling in hiPSC-epicardial cells. (**A**) Timeline qPCR analysis of *TFAP2A* in *PKP2*-corrected and c.2013delC hiPSC-epicardial cells. Data represented as relative FC to day 0 *PKP2*-corrected cells ($n = 3$ to 4). (**B**) Representative immunofluorescence staining for TFAP2A in day 80 *PKP2*-corrected and c.2013delC hiPSC-epicardial cells. (**C**) Representative Western blot analysis of TFAP2A protein in the indicated day 80 hiPSC-epicardial cells. GAPDH, glyceraldehyde-3-phosphate dehydrogenase. (**D**) qPCR analysis of fibro-fatty genes after *TFAP2A* knockdown in day 80 *PKP2* c.2013delC hiPSC-epicardial cells. Data represented as relative FC to scrambled siRNA indicated by the dashed line ($n = 4$ to 6). (**E**) Schematic of lentivirus-mediated *TFAP2A* overexpression in 1-month-old control hiPSC-epicardial cells. (**F**) Representative Western blot analysis of TFAP2A protein after viral transduction. (**G**) qPCR analysis of fat and fibroblast markers after *TFAP2A* overexpression. Data represented as relative FC to control lentivirus-treated cells indicated by the dashed line ($n = 3$ to 4). (**H**) Representative immunofluorescence staining for WT1 and α-SMA in control and *TFAP2A* lentivirus–transduced hiPSC-epicardial cells. (**I**) Representative bright-field images of Oil red O and hematoxylin staining in control and *TFAP2A* lentivirus–transduced hiPSC-epicardial cells. (**J**) Quantification of the Oil red O staining in (I). Data represented as relative FC to lenti-control ($n = 7$). (**K**) Representative histograms showing flow cytometric analysis of CD73 and CD29 in *PKP2*-corrected and c.2013delC hiPSC-epicardial cells at the indicated culture time points. Bar graphs show MFI (mean fluorescence intensity) ratio of test samples relatively compared to day 30 *PKP2*-corrected hiPSC-epicardial cells ($n = 2$). (**L**) qPCR analysis of *CDH1/CDH2* ratio in the culture timeline of *PKP2*-corrected and c.2013delC hiPSC-epicardial cells. Data represented as relative FC to day 0 *PKP2*-corrected cells ($n = 3$ to 4). (**M**) Control hiPSC-epicardial cells were triggered to undergo EMT and then transfected with *TFAP2A*-targeting siRNAs. qPCR analysis of the indicated genes is shown below. Data represented as relative FC to TGFβi and scrambled siRNA treatment indicated by the dashed line ($n = 5$ to 6). All data are means ± SEM. Statistical significance was evaluated using Student's *t* test in (A), (D), (G), and (J) to (L) and one-way analysis of variance (ANOVA) with Dunnett's multiple comparisons test in (M). Statistical comparisons in (M) were performed against TGFβ and si-scrambled group (versus TGFβi and si-scrambled presented by asterisks and versus TGFβ and si-*TFAP2A* presented by dollar symbols) (*/$$P < 0.05$; **/$$P < 0.01$; ***/$$$P < 0.001$; ****/$$$$P < 0.0001$). ND, not detected; cor, *PKP2* corrected.

significant reduction after 1 month in *PKP2* c.2013delC hiPSC-epicardial cells, further suggesting a mesenchymal transition (Fig. 4L; $P < 0.0001$). To investigate whether artificially induced EMT would promote a similar fibro-fatty phenotype, we cultured control hiPSC-epicardial cells in the presence of transforming growth factor–β (TGFβ), an inducer of epicardial EMT (*16*), which, as expected, promoted the expression of *TFAP2A* and fibro-fatty markers. However, *TFAP2A* suppression abolished this effect (Fig. 4M).

To further validate these findings, we used primary adult human atrial EPDCs obtained during extracorporeal bypass surgeries (fig. S13A). These cells adopt a cobblestone morphology and can undergo EMT into α-SMA$^+$ spindle-shaped cells upon TGFβ stimulation (fig. S13, B and F) (*23*). When cultured ex vivo, we observed that all desmosomal genes were expressed in EPDCs (fig. S13, C and D). Treatment of EPDCs with TGFβ significantly induced the expression of mesenchymal and fibroblast markers but did not affect fat markers (fig. S13G; $P < 0.05$). In line with our previous results in hiPSC-epicardial cells, silencing of *TFAP2A* led to a reduction in TGFβ-mediated EMT and fibrosis and a rescue of *WT1* mRNA expression. However, silencing of *PKP2* did not seem to enhance EMT or fibro-fatty gene expression (fig. S13, E to G). Together, these results suggest that loss of desmosomal proteins can alleviate epicardial quiescence, leading to epicardial activation, EMT, and cellular differentiation in a TFAP2A-dependent manner.

Epicardial cell transition is mutation independent

To exclude that our findings were mutation dependent, we obtained an additional hiPSC line with a different ACM-associated *PKP2* mutation (*PKP2* c.1849C>T) and generated its isogenic corrected control (fig. S14, A to H). Cells were differentiated into epicardial cells and maintained up to 4 months of culture (fig. S14, I and J). Corroborating our previous results, *PKP2* c.1849C>T hiPSC-epicardial cells showed a reduction of *WT1* and induction of *TFAP2A* and fibro-fatty markers after 80 days of culture (fig. S14K). However, the increase in *PPARG* expression and the spontaneous accumulation of lipid droplets in mutant cells were only observed after 4 months of culture (fig. S14, K to M). This is in line with the variable disease penetrance and remodeling that is seen in patients.

To validate the dependence of these findings on desmosomal gene defects, we knocked down the desmosomal genes *PKP2*, *DSP*, and *JUP* in control hiPSC-epicardial cells (Fig. 5A). *TFAP2A* as well as fibroblast and fat cell markers were strongly induced in *PKP2*, *DSP*, and *JUP* siRNA-treated samples (Fig. 5, B and C, and fig. S12C), recapitulating our findings in *PKP2*-mutant hiPSC-epicardial cells. To identify whether PKP2 reduction in other cardiac cells would trigger the same effect, we differentiated cardiomyocytes from *PKP2*-corrected and c.2013delC hiPSC lines and did not observe molecular or phenotypical differences after 1 month of culture (fig. S15, A to D). In addition, *PKP2* targeting in cardiomyocytes generated from control hiPSCs did not cause an induction of fibro-fatty markers, suggesting the transdifferentiation process to be cardiomyocyte independent (fig. S15E).

Cardiac explants from patients with ACM show subepicardial WT1 and TFAP2A expression

To explore the relevance of TFAP2A-mediated epicardial–to–fibro-fatty differentiation in ACM, we analyzed the abundance of WT1 and TFAP2A in explanted human hearts. Histological analysis of ventricular sections from patients with ACM harboring different *PKP2*, *DSP*, and phospholamban (*PLN*) mutations displayed replacement of healthy myocardium with massive fibro-fatty infiltrates labeled by the expression of the mesenchymal marker vimentin (VIM). These areas were covered with WT1-expressing cells, a phenomenon also observed in animal models after cardiac injury (*9*, *11*), suggesting epicardial activation in diseased hearts. This was associated with TFAP2A

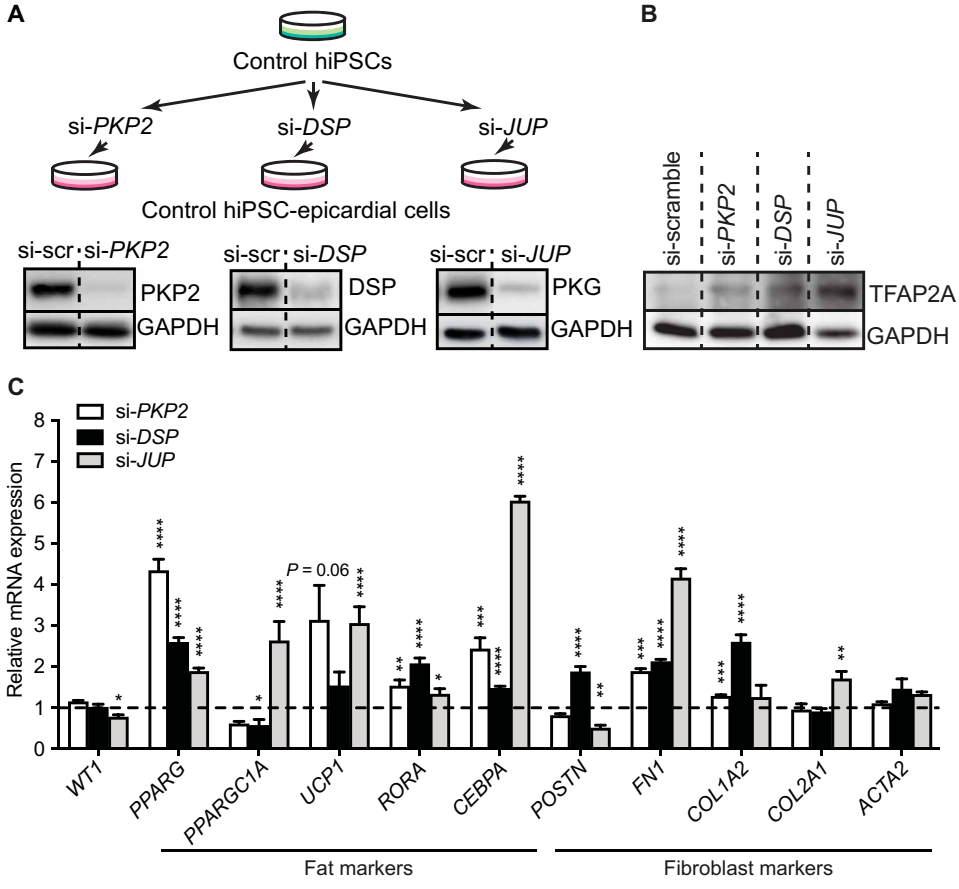

Fig. 5. Desmosomal gene suppression induces TFAP2A and fibro-fatty signaling. (**A**) Control hiPSC-epicardial cells were transfected with siRNAs targeting *PKP2*, *DSP*, or *JUP*. Knockdown was confirmed by the representative Western blots below. (**B**) Representative Western blot analysis of TFAP2A after knockdown experiments. (**C**) qPCR analysis of fibro-fatty genes after knockdown experiments. Data represented as relative FC compared to corresponding scrambled siRNA indicated by the dashed lines ($n = 5$ to 6). Data in (C) are means ± SEM. Statistical significance was evaluated using Student's *t* test (*$P < 0.05$; **$P < 0.01$; ***$P < 0.001$; ****$P < 0.0001$).

expression (Fig. 6A). Furthermore, Western blot analysis of additional ventricular samples from patients with ACM showed a trending increase in WT1 and TFAP2A expression alongside with reduced PKP2 amounts as compared to healthy controls (Fig. 6, B and C). These data further support a TFAP2A-mediated epicardial–to–fibro-fatty transition in patients with ACM.

DISCUSSION

Fibro-fatty replacement of healthy myocardium is a progressive characteristic of the remodeling process during ACM that correlates to disease severity and cardiac dysfunction (*1*). However, studying this process has been challenging due to the absence of substantial cardiac fibro-fatty deposits in ACM mouse models and limited in vitro systems. Here, we showed that epicardial differentiation contributes to the fibro-fatty phenotype seen in patients with ACM. In addition, we present TFAP2A as a key transcription factor mediating this process via EMT. Together, our results suggest that desmosomal structures are critical components to maintain epicardial integrity as epithelial cells, which, when lost, lead to the activation of the epicardium and its differentiation into fibroblasts and fat cells that can infiltrate the myocardium (fig. S16).

Cellular models to study fibro-fatty differentiation have largely depended on cultures exposed to lipogenic stimuli to trigger an adipogenic phenotype (*24*–*30*). Using hiPSC-epicardial cultures from patients with ACM, we showed the occurrence of spontaneous fibro-fatty differentiation without the requirement of external cues. This is likely due to a direct effect of reduced desmosomal gene expression as silencing of *PKP2*, *DSP*, and *JUP* triggered similar effects. This effect appeared to be specific for epicardial cells, because

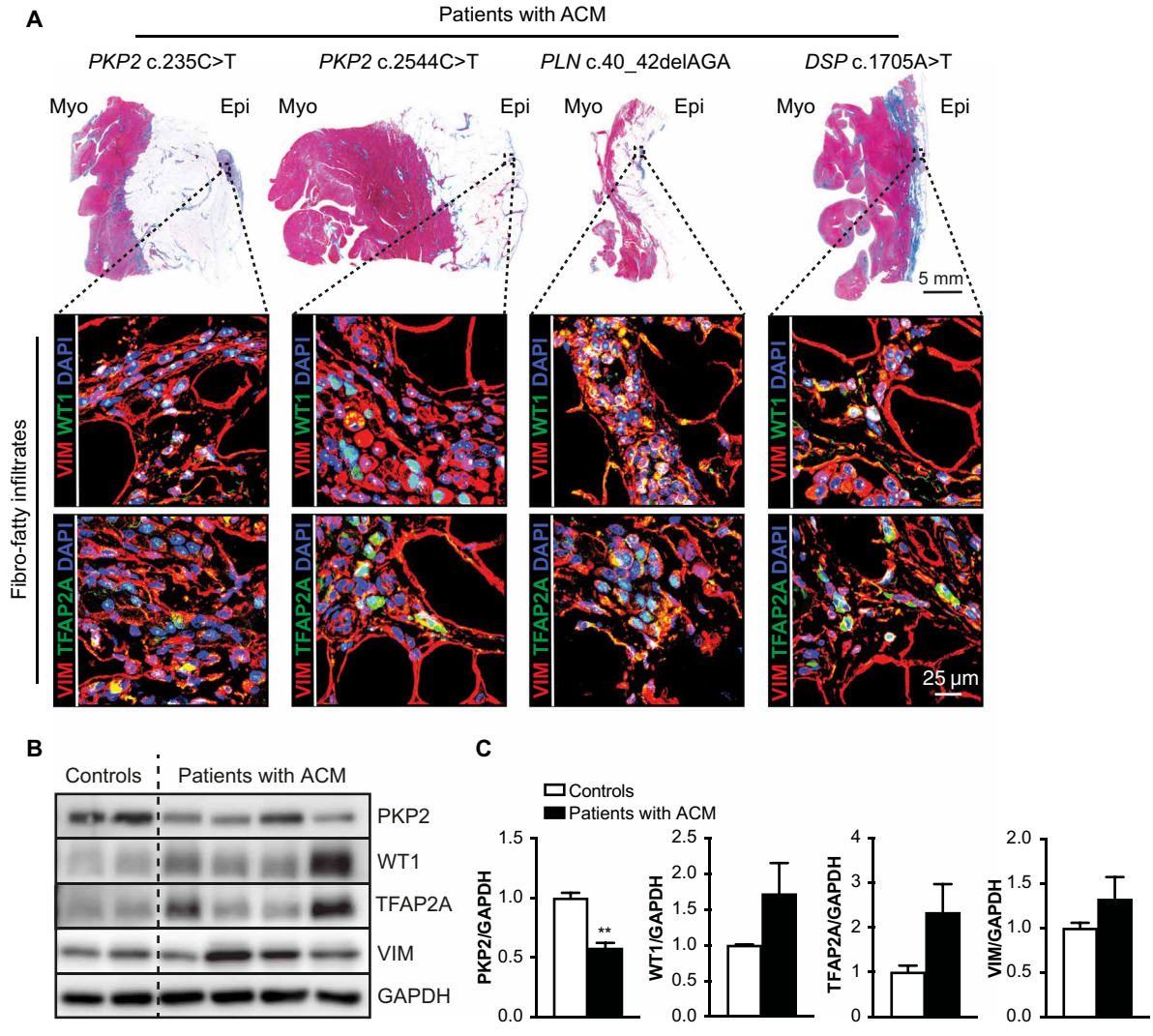

Fig. 6. Epicardial activation and TFAP2A induction in ACM hearts. (**A**) Top panels show Masson trichome staining of heart sections from patients with ACM carrying the indicated *PKP2*, *PLN*, and *DSP* mutations depicting myocardium in red, fibrosis in blue, and adipose tissue in white. Insets indicate fibro-fatty regions where immunofluorescence stainings for WT1, TFAP2A, and VIM were performed. (**B**) Western blot analysis of PKP2, WT1, TFAP2A, and VIM in cardiac tissue collected from left ventricles of controls and patients with ACM (*PKP2* c.235C>T, *PKP2* c.2386T>C, *PKP2* c.397C>T, and *PKP2* c.2544G>A). (**C**) Quantification of blots in (B) ($n = 2$ to 4). Data represented as relative FC compared to control hearts. Data in (C) are means ± SEM. Statistical significance was evaluated using Student's *t* test (**$P < 0.01$). Epi, epicardium; Myo, myocardium.

mutant hiPSC-cardiomyocytes harboring the same mutation did not show the propensity to undergo lipogenesis and fibro-fatty differentiation.

A previous study suggested a role for the epicardium in fibro-fatty replacement, as silencing of *Pkp2* in neonatal rat epicardial explants resulted in reduced E-cadherin expression, increased cellular proliferative rates, and differentiation into α-SMA$^+$ cells (*31*). Because these cells started accumulating lipids when cultured in an lipogenic milieu, the authors suggested that epicardial cells might act as adipocyte progenitors (*31*).

Several ACM mouse models have been developed to study disease pathophysiology and mechanisms [reviewed in (*5*, *6*)]. These models displayed common ACM features, such as desmosomal dysfunction, ventricular arrhythmias, and myocardial apoptosis. However, delineating the cellular origin of fat tissue has been difficult due to the limited potential of murine hearts to accumulate fat (*7*). Adipose tissue in mice is often confined to a small region in the heart, the atrial-ventricular groove. Epicardial lineage tracing models showed that this atrial-ventricular groove fat originates via epicardial EMT and activation of the PPARγ (peroxisome proliferator–activated receptor γ) pathway (*7*, *32*). A similar approach could show the epicardial origin of atrial adipocytes in a model of atrial fibrillation (*12*). This appeared to be due to a preprogrammed state of subsets of adult EPDCs toward either fibroblast or adipocyte cell fates, which, when activated, contribute to fibro-fatty infiltrations of diseased atria (*13*).

In the context of ACM, adipocytes in an ACM mouse model have been shown to arise from second heart field progenitors labeled by insulin gene enhancer protein (ISL1) and myocyte enhancer factor 2C (MEF2C) (*33*). Work from the same group later showed that platelet-derived growth factor receptor A$^+$ (PDGFRA$^+$) Thy-1 cell surface antigen (THY1) fibro-adipogenic progenitors gave rise to fibroblasts and adipocytes in these hearts (*34*). These results do not oppose ours, because Isl1$^+$ progenitors also give rise to epicardium (*35*) and PDGFRA$^+$ cells can be multipotent cells derived from the epicardium (*36*). In addition, in explanted ACM hearts, mesenchymal stromal cells were found to contribute to fibro-fatty cells that were suggested to originate from epicardial EMT (*37*). This was also confirmed by our observation of WT1$^+$ mesenchymal cells in subepicardial regions of ACM hearts. One recent study further supported our findings using an epicardial-specific *Dsp* deletion, which showed an EMT-driven epicardial origin of fibroblasts in mice (*38*). These data, together with the histological observation of fibro-fatty tissue extending from the epicardium towards the endocardium in patients with ACM (*15*), suggest a key role for the epicardium in fibro-fatty cellular transition.

Using scRNA-seq transcriptomics, we identified TFAP2A as a key transcription factor mediating epicardial–to–fibro-fatty transition upon desmosomal suppression or EMT induction. This was supported by the expression of TFAP2A in subepicardial infiltrates of patients with ACM. TFAP2A is a retinoic acid–inducible transcription factor that plays important roles in cell growth and differentiation. Both TFAP2A and desmosomal down-regulation have been linked to EMT and hence known to contribute to cancer development and metastasis (*19*, *39*). TFAP2A has also been implicated in TGFβ-mediated fibroblast-to-myofibroblast differentiation in response to TGFβ stimulation, which was further supported by the presence of TFAP2A binding sites in Smad2/3 promoter regions, important factors in TGFβ signaling (*22*). *TFAP2A* suppression in keratinocytes alters TGFβ-mediated gene transcription, a phenomenon that we also observed upon *TFAP2A* silencing in TGFβ-treated hiPSC-derived and primary adult epicardial cells (*40*). Other studies also identified TFAP2A as a master regulator of lipid droplet biogenesis (*21*) and as an essential component in preadipocyte to adipocyte differentiation (*20*). Using human atrial EPDCs as a primary model to validate our findings, we confirmed the role of TFAP2A in TGFβ-mediated EMT and fibrosis. However, we did not observe an adipogenic phenotype upon TGFβ stimulation or *PKP2* knockdown. This could potentially be explained by the atrial nature of these EPDCs, whereas we think that it is mainly the ventricular epicardial cells from ACM hearts that contribute to the fibro-fatty replacement. One other possibility would be the need for a stronger stressor to induce a fibro-fatty phenotype such as the intrinsic pathogenic mutations present in hiPSC-epicardial cells, which is difficult to introduce into primary cultures.

Currently, clinical management of ACM mainly relies on the administration of anti-arrhythmic drugs. However, no treatments are available to target the progressive fibro-fatty remodeling process, which acts as a substrate for ventricular arrhythmias (*3*, *4*). From a clinical perspective, the epicardium is an easily targetable tissue allowing for local delivery of drugs to the pericardial sac. Our data suggest that the therapeutic inhibition of epicardial TFAP2A could lead to a reduction of fibro-fatty replacement and might thereby prevent ACM disease progression.

However, there are some limitations to our work. Our findings rely on an EMT-driven phenotype in epicardial cells due to suppressed desmosomal gene expression. Although desmosomal gene mutations are the most frequent cause of ACM, mutations in non-desmosomal genes have also been reported to cause ACM. Therefore, our findings must be validated in hiPSC lines generated from patients with ACM carrying nondesmosomal gene mutations (*2*, *14*). Further studies will also have to indicate whether other cardiac disorders associated with cardiac fibro-fatty infiltrations, such as hypertrophic cardiomyopathy and myocardial infarction, could also potentially benefit from TFAP2A inhibition. Although the examination of the epicardium in explanted human hearts allows for an adequate validation of in vitro findings, this is problematic due to often occurring epicardial detachment during surgical dissection procedures. Furthermore, despite the potential of hiPSC-based modeling, the clinical impact of TFAP2A inhibition remains to be validated in larger animal models with a propensity to cardiac fibro-fatty development.

In conclusion, we used hiPSC technology to generate a human in vitro model system that can serve to study aspects of cardiac fibro-fatty remodeling during ACM and defined TFAP2A as a key factor regulating this process. Future studies will be directed at testing the therapeutic potential of epicardial inhibition of TFAP2A during fibro-fatty replacement in the human heart.

MATERIALS AND METHODS

Study design

This study was designed to exploit the potential of hiPSC-epicardial cells to undergo fibro-fatty differentiation in the setting of ACM. To investigate this, we (i) compared hiPSC-epicardial cells generated from patients with ACM and their corrected isogenic controls, (ii) used scRNA-seq to identify factors that might contribute to the phenotype observed, and (iii) validated our results using loss- and gain-of-function experiments and explanted human hearts. hiPSC

lines were obtained from patients with known pathogenic PKP2 mutations or from healthy donors as previously described (*29*, *41*). Adult human EPDCs were obtained during right atrial cannulation for extracorporeal bypass surgery (*23*) and were approved by the ethics committee of Leiden University Medical Center and conformed to the Declaration of Helsinki. Experiments on explanted human hearts were approved by the scientific advisory board of the biobank of the University Medical Center Utrecht, the Netherlands (protocol no. 12/387). Written informed consent was obtained or, in certain cases, waived by the ethics committee when obtaining informed consent was not possible due to death of the patient. The epicardial–to–fibro-fatty phenotype was assessed using transcriptomic, protein, and histological analyses. Measurements were not blinded. Different replicate numbers were used in each experiment, which were specified in figure legends.

Cell culture

Human *PKP2* c.2013delC, *PKP2* c.1849C>T, and control hiPSC lines were provided by H.-S. V. Chen at University of California San Diego (*29*), J. Wu at Stanford Cardiovascular Institute (supported by National Institutes of Health R24 HL117756), and M. Bellin and C. Freund at Leiden University Medical Center (*41*), respectively. hiPSCs were maintained in Essential 8 Medium (Thermo Fisher Scientific, A1517001) on Geltrex (Thermo Fisher Scientific, A1413302)–coated plates (*42*). The hiPSC-epicardial cell differentiation protocol was adapted and optimized from Bao *et al.* (*16*). Briefly, hiPSCs were cultured until confluent in Essential 8 Medium on Geltrex-coated flasks. On day 0, medium was replaced with differentiation medium [RPMI medium (Thermo Fisher Scientific, 72400021) containing L-ascorbic acid (0.2 mg/ml; Sigma-Aldrich, A8960)] and supplied with 4 μM CHIR99021 (Sigma-Aldrich, SML1046) to promote mesoderm differentiation. On day 2, medium was replaced with differentiation medium containing 5 μM IWP2 (Inhibitor of Wnt Production-2) (Millipore, 681671) to direct cardiac progenitor cell differentiation, which was then changed to differentiation medium alone on day 4. Cardiac progenitor cells were generated on day 6 at which point cells were dissociated using StemPro Accutase Cell Dissociation Reagent (Thermo Fisher Scientific, A1110501) containing 2.5% trypsin (Thermo Fisher Scientific, 15090046) and subsequently cultured in LaSR basal medium [Advanced Dulbecco's modified Eagle's medium (DMEM)/F-12 (Thermo Fisher Scientific, 12634010) containing L-ascorbic acid (0.1 mg/ml; Sigma-Aldrich, A8960)]. On day 7, medium was replaced with LaSR basal medium containing 4 μM CHIR99021 to promote epicardial cell fate. Nonaddition of CHIR99021 at day 7 promoted a cardiomyocyte cell lineage. On day 9, medium was changed to LaSR basal medium. From day 12 onward, cells were maintained in LaSR basal medium containing TGFβ inhibitor (Stemgent, 04-0014) to prevent spontaneous EMT and split whenever confluent. Thiazovivin (2 μM; Millipore, 420220) was added at every cell split. The hiPSC-cardiomyocyte differentiation protocol was adapted from Burridge *et al.* (*42*). Briefly, cells were treated similarly to hiPSC-epicardial cells up to day 4. On day 6, cells were refreshed with differentiation medium for 2 days. On day 8 and every 2 to 3 days thereafter, medium was changed to cardio culture medium [RPMI medium (Thermo Fisher Scientific, 72400021) containing B-27 supplement (Thermo Fisher Scientific, 17504001)]. Around day 14, cells were replated at a lower density in cardio culture containing 2 μM thiazovivin and subsequently cultured in cardio selection medium [RPMI no glucose (Biological Industries 01-101-1A), 4 mM lactate-Hepes, recombinant human albumin (0.5 mg/ml), and L-ascorbic acid (0.2 mg/ml)] for 4 days. Cells were subsequently maintained in cardio culture medium.

CRISPR-Cas9 targeting

Single-guide RNAs were selected based on the CCTop–CRISPR/Cas9 target online predictor tool (*43*) and cloned into pSpCas9(BB)-2A-GFP (PX458) (Addgene, 48138). To correct the *PKP2* c.2013delC and *PKP2* c.1849C>T variants, we designed single-stranded oligodeoxynucleotides (Ultramer, Integrated DNA Technologies) according to the observations of Richardson *et al.* (*44*). Besides the intended mutation, the asymmetric DNA template contained an additional synonymous mutation that destroys the protospacer adjacent motif (PAM) sequence upon successful targeting, thereby preventing Cas9 from recutting (tables S1 and S2). For transfection experiments, mutant hiPSCs were pretreated with Essential 8 Medium supplemented with 2 μM thiazovivin for 1 hour before transfection. Next, hiPSCs were dissociated with 1× TrypLE Express Enzyme (Thermo Fisher Scientific, 12605010), and cell number was determined. The Lonza Nucleofector System (Lonza, VAPH-5012; program: human embryonic stem cells, A023) was used to transfect 2×10^6 of hiPSCs with 10 μg of PX458 vector and 1 μg of single-stranded oligodeoxynucleotides according to the manufacturer's instructions. After nucleofection, cells were seeded into Geltrex (Thermo Fisher Scientific, A1413302)–coated plates for 24 hours. Green fluorescent protein$^+$ (GFP$^+$) cells were single-cell sorted using the BD FACSJazz Cell Sorter (BD Biosciences) into 96-well plates coated with mouse embryonic fibroblasts. Sorted cells were maintained in Essential 8 Medium for 2 weeks and were subsequently passaged for maintenance and genotyping. To genotype the expanded clones, genomic DNA was isolated from cells using standard ethanol precipitation methods. The genomic region of interest containing the mutation was polymerase chain reaction (PCR) amplified using GoTaq Green Master Mix (Promega, M7823). PCR products were sent for Sanger sequencing (Macrogen) and analyzed with SnapGene Viewer (SnapGene). For successfully corrected clones, we analyzed the top-predicted off-target sites generated by CCTop–CRISPR/Cas9 target online predictor tool. Lists of top off target sites and sequencing primers are provided in table S3.

Karyotyping

hiPSCs were incubated for 3 hours in Essential 8 Medium with colcemid (0.05 μg/ml; Thermo Fisher Scientific, 152120-012) and subsequently collected and treated with 0.075 M KCl (1 ml) for 30 min at 37°C. A few drops of methanol:acetic acid (3:1) were added to the cell suspension. Cell pellet was collected, resuspended in 1 ml of methanol:acetic acid, and incubated for 20 min at room temperature to fix the cells. This step was repeated twice. Last, cells were dropped onto glass slides from ±30 cm height, air-dried, and covered with ProLong Gold Antifade reagent with 4′,6-diamidino-2-phenylindole (DAPI) (Thermo Fisher Scientific, P36935) and a coverslip. Slides were imaged using the Leica TCS SPE confocal microscope (Leica Microsystems).

Immunofluorescence staining

Cells were fixed with 4% paraformaldehyde, blocked with 4% goat serum, and incubated for 1 hour with primary antibodies (table S4). Cells were subsequently stained with the corresponding Alexa Fluor secondary antibodies (Thermo Fisher Scientific) for 1 hour and then with DAPI (1:1000) for 5 min and lastly mounted for imaging.

Human ACM hearts were sectioned at 4 μm and left to stretch in a 42°C water bath. Next, sections were picked with coated glass slides and incubated overnight in a 58°C stove. On the next day, sections were deparaffinized in xylene, rehydrated, and rinsed in demi water. Subsequently, antigen retrieval was done in boiling EDTA buffer (pH 9) for 20 min. Slides were cooled down to 37°C and incubated with primary antibodies (table S4) overnight at 4°C. On the next day, slides were incubated with the corresponding Alexa Fluor secondary antibodies (Thermo Fisher Scientific) for 1 hour at room temperature. Last, slides were stained with DAPI (1:1000) for 5 min and mounted. Imaging was done using the Leica TCS SPE confocal microscope, and images were analyzed using Fiji software.

Western blot

Proteins were isolated from cells using radioimmunoprecipitation assay buffer [50 mM tris-HCl (pH 7.5), 150 mM NaCl, 0.1% SDS, 0.5% sodium deoxycholate (Sigma-Aldrich), 1% Triton X-100 (Sigma-Aldrich), and protease inhibitor (Roche)], and protein concentration was determined using Bradford Assay (Bio-Rad). SDS–polyacrylamide gel electrophoresis and Western blot were performed using Mini-PROTEAN Tetra Vertical Electrophoresis Cell with Mini Trans-Blot (Bio-Rad). Membranes were blocked in 3% nonfat dry milk and subsequently incubated overnight at 4°C with primary antibodies (table S4). On the next day, blots were washed and incubated with peroxidase-conjugated AffiniPure rabbit anti-mouse immunoglobulin G (IgG) (Jackson ImmunoResearch, 315-035-003) and goat anti-rabbit IgG secondary antibodies (Jackson ImmunoResearch, 111-035-003) for 45 min, and proteins were visualized using enhanced chemiluminescence solution (Bio-Rad, 170-5061) on the LAS 4000 software program. Western blots were quantified using Fiji software.

Flow cytometry

Cells were fixed with 70% ethanol and incubated in blocking buffer (phosphate-buffered saline, 5% fetal bovine serum, 1% bovine serum albumin, and 0.5% Triton X-100) for 10 min at 4°C. Cells were subsequently incubated with primary antibodies (table S4) for 1 hour and then the corresponding Alexa Fluor secondary antibodies (Thermo Fisher Scientific) for 30 min at 4°C. Flow cytometry was performed using FACSAria SORP (BD Biosciences), and plots were analyzed using FlowJo software.

RNA isolation and quantitative real-time PCR

Total RNA was isolated from cells using the RNeasy Mini Kit (QIAGEN, 74104) and reverse-transcribed into cDNA using the iScript cDNA Synthesis Kit (Bio-Rad, 1708891) according to the manufacturer's instructions. Quantitative PCR (qPCR) was performed using the iQ SYBR Green Supermix (Bio-Rad, 170-8885) with the CFX96 Real-Time PCR instrument (Bio-Rad). Transcript amounts were normalized for endogenous loading. Sequences of primers used for qPCR are provided in table S5.

Bulk RNA-seq

RNA-seq was performed on 1-month-old *PKP2* c.1849C>T and corrected hiPSC-epicardial cells. RNA was isolated as previously described, and Poly-A–purified RNA-seq libraries were prepared using the TruSeq Stranded mRNA Library Prep Kit (Illumina) according to the manufacturer's protocol. Next, strand-specific single-end 75–base pair (bp) reads were generated on an Illumina NextSeq 500. Samples were sequenced to an average depth of 44 ± 3.4 million reads (mean ± SD). Reads were mapped to human reference genome GRCh37 and quantified against the corresponding Ensembl gene annotation list using STAR v 2.4.2a. Differential expression was calculated using DESeq2 v1.2 with pooled dispersion estimates (*45*). For downstream ClueGO GO analysis, genes were selected that were significantly down- and up-regulated by a $\log_2$ FC of at least −2 or 2, respectively, and with a P value lower than 0.05 after Benjamini-Hochberg correction. To determine expression of wild-type and mutant alleles, a custom-made RegEx-based script was used in Python v2.7. All reads in raw FASTQ files were searched for a 20-bp sequence overlapping locus of the deletion mutation or inserted base pair [AAAAGAGCAA(C)CCCAAGGGC]. Per sample, number of reads containing the mutated and wild-type sequence were counted separately and converted to a percentage of the total number of reads containing one of the two sequences.

Oil red O staining

Cells were stained using the Lipid Oil red O staining kit (Sigma-Aldrich, MAK194) according to the manufacturer's instructions. Slides were visualized using a Leica DM4000 microscope and a Zeiss Axioskop 2 Plus with an AxioCam HRc. An average percentage of Oil red O–positive area per field was quantified using Fiji software.

Single-cell RNA-seq

scRNA-seq was performed by Single Cell Discoveries according to an adapted version of the SORT-seq (SOrting and Robot-assisted Transcriptome SEQuencing) protocol (*46*) with primers described in (*47*). In short, day 70 *PKP2*-corrected and c.2013delC hiPSC-epicardial cells were dissociated and single-cell sorted using the BD FACSJazz Cell Sorter (BD Biosciences) into 384-well plates containing 384 primers and mineral oil (Sigma-Aldrich). After sorting, plates were snap-frozen on dry ice and stored at −80°C. For amplification, cells were heat-lysed at 65°C followed by cDNA synthesis using the CEL-Seq2 (Cell Expression by Linear amplification and Sequencing-2) protocol (*48*) and robotic liquid handling platforms. After second-strand cDNA synthesis, the barcoded material was pooled into libraries of 384 cells and amplified using in vitro transcription. After amplification, the rest of the CEL-Seq2 protocol was followed for preparation of the amplified cDNA library, using TruSeq small RNA primers (Illumina). The DNA library was paired-end sequenced on an Illumina NextSeq 500, high output, with a 1 × 75 bp Illumina kit (read 1: 26 cycles, index read: 6 cycles, and read 2: 60 cycles).

Single-cell data analysis

During sequencing, read 1 was assigned 26 bp and was used for identification of the Illumina library barcode, cell barcode, and unique molecular identifier (UMI). Read 2 was assigned 60 bp and used to map to the reference transcriptome of Hg19 with Burrows-Wheeler Aligner (*49*). Data were demultiplexed, and transcript counts were calculated from UMI counts using binomial statistics as described in (*50*). Single-cell transcriptomics analysis was done using the Monocle 2 package (*51*, *52*) version 2.10.1, following the Monocle 2 manual (http://cole-trapnell-lab.github.io/monocle-release/docs/). In total, two 384-well plates with *PKP2* c.2013delC cells and two 384-well plates with *PKP2*-corrected cells were sequenced. Mitochondrial transcript counts were removed, as were genes expressed in less than 10 cells. Consecutively, cells with a

remaining transcript count ≤5000 were removed. This resulted in the selection of 621 *PKP2* c.2013delC single cells and 556 *PKP2*-corrected single cells and an overall total transcript count of 33,681,317 coming from 15,709 genes. Applying the analysis steps suggested by the Monocle 2 manual, t-distributed stochastic neighbor embedding (t-SNE) maps were generated by the application of principal components analysis (and back transformation using only the first six principal components) followed by application of t-SNE dimensionality reduction. Cells were clustered by the Monocle 2 function clusterCells (using the default densityPeak method and setting num_clusters = NULL); this function applies the densityClust algorithm. Differential gene expression for the clusters was determined by the Monocle 2 function clustering DEG_genes. Transcription factors in differentially expressed genes were identified using a previously published list of human transcription factors (*53*). Then, the branch plot and pseudotime assignment were determined by the Monocle 2 functions reduceDimensions (DDRTree method) and orderCells, respectively.

siRNA transfection

siRNA trilencers were purchased from OriGene to target *TFAP2A* (SR304787), *PKP2* (SR303544), *DSP* (SR301285), and *JUP* (SR302502). A corresponding scrambled siRNA was used as a control (SR30002). A total of 10 nM siRNA trilencer was used for transfection using Lipofectamine 3000 (Life Technologies, L3000008) according to the manufacturer's instructions.

Lentiviral production and transduction

TFAP2A coding sequence was cloned into the transfer vector pLVX-IRES-Hyg (Clontech, 632185), and 7 μg was subsequently transfected into HEK293T cells along with 7 μg of the packaging plasmid psPAX2 (Addgene, 12260) and 3 μg of the envelope plasmid pMD2.G (Addgene, 12259) using polyethylenimine (Polysciences, 23966). Supernatant containing viral particles was collected after 1 and 2 days and used to transduce control hiPSC-epicardial cells. Cells were harvested after 3 days for RNA, protein, and histological analysis.

EMT induction

hiPSC-epicardial cells were triggered to undergo EMT through the addition of TGFβ (5 ng/ml; PeproTech, 100-21) in LaSR basal media for two consecutive days. Cells were subsequently treated for 24 hours with 10 nM *TFAP2A*-targeting siRNAs (OriGene, SR304787), and a scrambled siRNA was used as a control.

Isolation and culture of human EPDCs

Adult human atrial samples were collected as redundant material during right atrial cannulation for extracorporeal bypass surgery. Samples were collected as surgical waste after informed consent. Experiments were approved by the ethics committee of Leiden University Medical Center and conformed to the Declaration of Helsinki. Isolation of adult EPDCs was performed according to the protocol described in (*23*). Briefly, EPDCs were collected by peeling off the epicardium from the underlying myocardium. Tissue was cut into small pieces and digested through three rounds of 10 min incubation in 1:1 trypsin 0.25% (Serva) and EDTA (USH products) at 37°C. The cell suspension was then passed through a series of syringes of decreasing size (19 to 22 gauge), subsequently passed through a 100-μm cell strainer (BD Falcon), and plated on gelatin-coated dishes (Sigma-Aldrich). EPDCs were lastly cultured on gelatin-coated plates in a 1:1 mixture of DMEM, low glucose (Thermo Fisher Scientific) and Medium 199 (Thermo Fisher Scientific) supplemented with 10% heat-inactivated fetal calf serum (Gibco), and 100 U/ml penicillin/streptomycin (Gibco). To prevent cells from undergoing EMT, 5 μM SB431542 (Tocris Bioscience) was added. For knockdown experiments, cells were treated with scramble (OriGene, SR30002) or *TFAP2A* siRNA (OriGene, SR304787) for 24 hours followed by stimulation with TGFβ (1 ng/ml) for another 24 hours to promote EMT.

Samples from patients with ACM

The study met the criteria of the code of proper use of human tissue in the Netherlands. Collection of explanted human hearts was approved by the scientific advisory board of the biobank of the University Medical Center Utrecht, the Netherlands (protocol no. 12/387). Written informed consent was obtained or waived by the ethics committee when obtaining informed consent was not possible due to death of the patient. In this study, we obtained tissue from the left ventricular free wall from explanted human hearts for Western blot analysis and immunostaining.

Statistical analysis

Data were analyzed using PRISM (GraphPad Software Inc., version 6), and results were presented as means ± SEM. Number of samples (n) and the statistical test used for each analysis are indicated in figure legends. $P < 0.05$ was considered significant.

SUPPLEMENTARY MATERIALS

www.science.org/doi/10.1126/scitranslmed.abf2750
Figs. S1 to S16
Tables S1 to S5
Data file S1

View/request a protocol for this paper from *Bio-protocol*.

REFERENCES AND NOTES

1. D. Corrado, M. S. Link, H. Calkins, Arrhythmogenic right ventricular cardiomyopathy. *N. Engl. J. Med.* **376**, 61–72 (2017).
2. J. A. Groeneweg, A. Bhonsale, C. A. James, A. S. te Riele, D. Dooijes, C. Tichnell, B. Murray, A. C. Wiesfeld, A. C. Sawant, B. Kassamali, D. E. Atsma, P. G. Volders, N. M. de Groot, K. de Boer, S. L. Zimmerman, I. R. Kamel, J. F. van der Heijden, S. D. Russell, M. J. Cramer, R. J. Tedford, P. A. Doevendans, T. A. van Veen, H. Tandri, A. A. Wilde, D. P. Judge, J. P. van Tintelen, R. N. Hauer, H. Calkins, Clinical presentation, long-term follow-up, and outcomes of 1001 arrhythmogenic right ventricular dysplasia/cardiomyopathy patients and family members. *Circ. Cardiovasc. Genet.* **8**, 437–446 (2015).
3. T. De Coster, P. Claus, I. V. Kazbanov, P. Haemers, R. Willems, K. R. Sipido, A. V. Panfilov, Arrhythmogenicity of fibro-fatty infiltrations. *Sci. Rep.* **8**, 2050 (2018).
4. G. Thiene, D. Corrado, C. Basso, Arrhythmogenic right ventricular cardiomyopathy/dysplasia. *Orphanet J. Rare Dis.* **2**, 45 (2007).
5. K. M. Austin, M. A. Trembley, S. F. Chandler, S. P. Sanders, J. E. Saffitz, D. J. Abrams, W. T. Pu, Molecular mechanisms of arrhythmogenic cardiomyopathy. *Nat. Rev. Cardiol.* **16**, 519–537 (2019).
6. B. Gerull, A. Brodehl, Genetic animal models for arrhythmogenic cardiomyopathy. *Front. Physiol.* **11**, 624 (2020).
7. Y. Yamaguchi, S. Cavallero, M. Patterson, H. Shen, J. Xu, S. R. Kumar, H. M. Sucov, Adipogenesis and epicardial adipose tissue: A novel fate of the epicardium induced by mesenchymal transformation and PPARγ activation. *Proc. Natl. Acad. Sci. U.S.A.* **112**, 2070–2075 (2015).
8. A. von Gise, W. T. Pu, Endocardial and epicardial epithelial to mesenchymal transitions in heart development and disease. *Circ. Res.* **110**, 1628–1645 (2012).
9. B. Zhou, L. B. Honor, H. He, Q. Ma, J.-H. Oh, C. Butterfield, R.-Z. Lin, J. M. Melero-Martin, E. Dolmatova, H. S. Duffy, A. Gise, P. Zhou, Y. W. Hu, G. Wang, B. Zhang, L. Wang, J. L. Hall, M. A. Moses, F. X. McGowan, W. T. Pu, Adult mouse epicardium modulates myocardial injury by secreting paracrine factors. *J. Clin. Invest.* **121**, 1894–1904 (2011).

10. A. C. Gittenberger-de Groot, E. M. Winter, R. E. Poelmann, Epicardium-derived cells (EPDCs) in development, cardiac disease and repair of ischemia. *J. Cell. Mol. Med.* **14**, 1056–1060 (2010).
11. F. Limana, C. Bertolami, A. Mangoni, A. Di Carlo, D. Avitabile, D. Mocini, P. Iannelli, R. De Mori, C. Marchetti, O. Pozzoli, C. Gentili, A. Zacheo, A. Germani, M. C. Capogrossi, Myocardial infarction induces embryonic reprogramming of epicardial c-kit(+) cells: Role of the pericardial fluid. *J. Mol. Cell. Cardiol.* **48**, 609–618 (2010).
12. N. Suffee, T. Moore-Morris, P. Farahmand, C. Rucker-Martin, G. Dilanian, M. Fradet, D. Sawaki, G. Derumeaux, P. LePrince, K. Clement, I. Dugail, M. Puceat, S. N. Hatem, Atrial natriuretic peptide regulates adipose tissue accumulation in adult atria. *Proc. Natl. Acad. Sci. U.S.A.* **114**, E771–E780 (2017).
13. N. Suffee, T. Moore-Morris, B. Jagla, N. Mougenot, G. Dilanian, M. Berthet, J. Proukhnitzky, P. Le Prince, D. A. Tregouet, M. Puceat, S. N. Hatem, Reactivation of the epicardium at the origin of myocardial fibro-fatty infiltration during the atrial cardiomyopathy. *Circ. Res.* **126**, 1330–1342 (2020).
14. E. Lazzarini, J. D. Jongbloed, K. Pilichou, G. Thiene, C. Basso, H. Bikker, B. Charbon, M. Swertz, J. P. van Tintelen, P. A. van der Zwaag, The ARVD/C genetic variants database: 2014 update. *Hum. Mutat.* **36**, 403–410 (2015).
15. S. Sepehrkhouy, J. M. I. H. Gho, R. van Es, M. Harakalova, N. de Jonge, D. Dooijes, J. J. van der Smagt, M. P. Buijsrogge, R. N. W. Hauer, R. Goldschmeding, R. A. de Weger, F. W. Asselbergs, A. Vink, Distinct fibrosis pattern in desmosomal and phospholamban mutation carriers in hereditary cardiomyopathies. *Heart Rhythm* **14**, 1024–1032 (2017).
16. X. Bao, X. Lian, T. Qian, V. J. Bhute, T. Han, S. P. Palecek, Directed differentiation and long-term maintenance of epicardial cells derived from human pluripotent stem cells under fully defined conditions. *Nat. Protoc.* **12**, 1890–1900 (2017).
17. D. T. Paik, L. Tian, J. Lee, N. Sayed, I. Y. Chen, S. Rhee, J. W. Rhee, Y. Kim, R. C. Wirka, J. W. Buikema, S. M. Wu, K. Red-Horse, T. Quertermous, J. C. Wu, Large-scale single-cell RNA-Seq reveals molecular signatures of heterogeneous populations of human induced pluripotent stem cell-derived endothelial cells. *Circ. Res.* **123**, 443–450 (2018).
18. C. E. Friedman, Q. Nguyen, S. W. Lukowski, A. Helfer, H. S. Chiu, J. Miklas, S. Levy, S. Suo, J.-D. J. Han, P. Osteil, G. Peng, N. Jing, G. J. Baillie, A. Senabouth, A. N. Christ, T. J. Bruxner, C. E. Murry, E. S. Wong, J. Ding, Y. Wang, J. Hudson, H. Ruohola-Baker, Z. Bar-Joseph, P. P. L. Tam, J. E. Powell, N. J. Palpant, Single-cell transcriptomic analysis of cardiac differentiation from human PSCs reveals HOPX-dependent cardiomyocyte maturation. *Cell Stem Cell* **23**, 586–598.e8 (2018).
19. Y. Dimitrova, A. J. Gruber, N. Mittal, S. Ghosh, B. Dimitriades, D. Mathow, W. A. Grandy, G. Christofori, M. Zavolan, TFAP2A is a component of the ZEB1/2 network that regulates TGFB1-induced epithelial to mesenchymal transition. *Biol. Direct* **12**, 8 (2017).
20. W. Guo, J. Chen, Y. Yang, J. Zhu, J. Wu, Epigenetic programming of Dnmt3a mediated by AP2α is required for granting preadipocyte the ability to differentiate. *Cell Death Dis.* **7**, e2496 (2016).
21. C. C. Scott, S. Vossio, J. Rougemont, J. Gruenberg, TFAP2 transcription factors are regulators of lipid droplet biogenesis. *eLife* **7**, e36330 (2018).
22. G. R. Ross, S. Edwards, C. Warner, P. Homar, F. X. Downey, L. Emelyanova, F. Rizvi, A. Jahangir, Deletion of transcription factor AP-2α gene attenuates fibroblast differentiation into myofibroblast. *J. Cell. Mol. Med.* **23**, 6494–6498 (2019).
23. E. Dronkers, A. T. Moerkamp, T. van Herwaarden, M. J. Goumans, A. M. Smits, The isolation and culture of primary epicardial cells derived from human adult and fetal heart specimens. *J Vis Exp* , 57370 (2018).
24. J.-Y. Wen, C.-Y. Wei, K. Shah, J. Wong, C. Wang, H.-S. Chen, Maturation-based model of arrhythmogenic right ventricular dysplasia using patient-specific induced pluripotent stem cells. *Circ. J.* **79**, 1402–1408 (2015).
25. S. N. Chen, P. Gurha, R. Lombardi, A. Ruggiero, J. T. Willerson, A. J. Marian, The hippo pathway is activated and is a causal mechanism for adipogenesis in arrhythmogenic cardiomyopathy. *Circ. Res.* **114**, 454–468 (2014).
26. O. Caspi, I. Huber, A. Gepstein, G. Arbel, L. Maizels, M. Boulos, L. Gepstein, Modeling of arrhythmogenic right ventricular cardiomyopathy with human induced pluripotent stem cells. *Circ. Cardiovasc. Genet.* **6**, 557–568 (2013).
27. T. Dorn, J. Kornherr, E. I. Parrotta, D. Zawada, H. Ayetey, G. Santamaria, L. Iop, E. Mastantuono, D. Sinnecker, A. Goedel, R. J. Dirschinger, I. My, S. Laue, T. Bozoglu, C. Baarlink, T. Ziegler, E. Graf, R. Hinkel, G. Cuda, S. Kaab, A. A. Grace, R. Grosse, C. Kupatt, T. Meitinger, A. G. Smith, K. L. Laugwitz, A. Moretti, Interplay of cell-cell contacts and RhoA/MRTF-A signaling regulates cardiomyocyte identity. *EMBO J.* **37**, e98133 (2018).
28. E. Garcia-Gras, R. Lombardi, M. J. Giocondo, J. T. Willerson, M. D. Schneider, D. S. Khoury, A. J. Marian, Suppression of canonical Wnt/β-catenin signaling by nuclear plakoglobin recapitulates phenotype of arrhythmogenic right ventricular cardiomyopathy. *J. Clin. Invest.* **116**, 2012–2021 (2006).
29. C. Kim, J. Wong, J. Wen, S. Wang, C. Wang, S. Spiering, N. G. Kan, S. Forcales, P. L. Puri, T. C. Leone, J. E. Marine, H. Calkins, D. P. Kelly, D. P. Judge, H.-S. V. Chen, Studying arrhythmogenic right ventricular dysplasia with patient-specific iPSCs. *Nature* **494**, 105–110 (2013).
30. D. Ma, H. Wei, J. Lu, S. Ho, G. Zhang, X. Sun, Y. Oh, S. H. Tan, M. L. Ng, W. Shim, P. Wong, R. Liew, Generation of patient-specific induced pluripotent stem cell-derived cardiomyocytes as a cellular model of arrhythmogenic right ventricular cardiomyopathy. *Eur. Heart J.* **34**, 1122–1133 (2013).
31. S. A. Matthes, S. Taffet, M. Delmar, Plakophilin-2 and the migration, differentiation and transformation of cells derived from the epicardium of neonatal rat hearts. *Cell Commun. Adhes.* **18**, 73–84 (2011).
32. Q. Liu, X. Huang, J. H. Oh, R. Z. Lin, S. Duan, Y. Yu, R. Yang, J. Qiu, J. M. Melero-Martin, W. T. Pu, B. Zhou, Epicardium-to-fat transition in injured heart. *Cell Res.* **24**, 1367–1369 (2014).
33. R. Lombardi, J. Dong, G. Rodriguez, A. Bell, T. K. Leung, R. J. Schwartz, J. T. Willerson, R. Brugada, A. J. Marian, Genetic fate mapping identifies second heart field progenitor cells as a source of adipocytes in arrhythmogenic right ventricular cardiomyopathy. *Circ. Res.* **104**, 1076–1084 (2009).
34. R. Lombardi, S. N. Chen, A. Ruggiero, P. Gurha, G. Z. Czernuszewicz, J. T. Willerson, A. J. Marian, Cardiac fibro-adipocyte progenitors express desmosome proteins and preferentially differentiate to adipocytes upon deletion of the desmoplakin gene. *Circ. Res.* **119**, 41–54 (2016).
35. B. Zhou, A. von Gise, Q. Ma, J. Rivera-Feliciano, W. T. Pu, Nkx2-5- and Isl1-expressing cardiac progenitors contribute to proepicardium. *Biochem. Biophys. Res. Commun.* **375**, 450–453 (2008).
36. J. J. Chong, V. Chandrakanthan, M. Xaymardan, N. S. Asli, J. Li, I. Ahmed, C. Heffernan, M. K. Menon, C. J. Scarlett, A. Rashidianfar, C. Biben, H. Zoellner, E. K. Colvin, J. E. Pimanda, A. V. Biankin, B. Zhou, W. T. Pu, O. W. Prall, R. P. Harvey, Adult cardiac-resident MSC-like stem cells with a proepicardial origin. *Cell Stem Cell* **9**, 527–540 (2011).
37. E. Sommariva, S. Brambilla, C. Carbucicchio, E. Gambini, V. Meraviglia, A. Dello Russo, F. M. Farina, M. Casella, V. Catto, G. Pontone, M. Chiesa, I. Stadiotti, E. Cogliati, A. Paolin, N. Ouali Alami, C. Preziuso, G. d'Amati, G. I. Colombo, A. Rossini, M. C. Capogrossi, C. Tondo, G. Pompilio, Cardiac mesenchymal stromal cells are a source of adipocytes in arrhythmogenic cardiomyopathy. *Eur. Heart J.* **37**, 1835–1846 (2016).
38. P. Yuan, S. M. Cheedipudi, L. Rouhi, S. Fan, L. Simon, Z. Zhao, K. Hong, P. Gurha, A. J. Marian, Single-cell RNA sequencing uncovers paracrine functions of the epicardial-derived cells in arrhythmogenic cardiomyopathy. *Circulation* **143**, 2169–2187 (2021).
39. M. Chidgey, C. Dawson, Desmosomes: A role in cancer? *Br. J. Cancer* **96**, 1783–1787 (2007).
40. D. Koinuma, S. Tsutsumi, N. Kamimura, H. Taniguchi, K. Miyazawa, M. Sunamura, T. Imamura, K. Miyazono, H. Aburatani, Chromatin immunoprecipitation on microarray analysis of Smad2/3 binding sites reveals roles of ETS1 and TFAP2A in transforming growth factor β signaling. *Mol. Cell. Biol.* **29**, 172–186 (2009).
41. M. Zhang, C. D'Aniello, A. O. Verkerk, E. Wrobel, S. Frank, D. Ward-van Oostwaard, I. Piccini, C. Freund, J. Rao, G. Seebohm, D. E. Atsma, E. Schulze-Bahr, C. L. Mummery, B. Greber, M. Bellin, Recessive cardiac phenotypes in induced pluripotent stem cell models of Jervell and Lange-Nielsen syndrome: Disease mechanisms and pharmacological rescue. *Proc. Natl. Acad. Sci. U.S.A.* **111**, E5383–E5392 (2014).
42. P. W. Burridge, E. Matsa, P. Shukla, Z. C. Lin, J. M. Churko, A. D. Ebert, F. Lan, S. Diecke, B. Huber, N. M. Mordwinkin, J. R. Plews, O. J. Abilez, B. Cui, J. D. Gold, J. C. Wu, Chemically defined generation of human cardiomyocytes. *Nat. Methods* **11**, 855–860 (2014).
43. M. Stemmer, T. Thumberger, M. Del Sol Keyer, J. Wittbrodt, J. L. Mateo, CCTop: An intuitive, flexible and reliable CRISPR/Cas9 target prediction tool. *PLOS ONE* **10**, e0124633 (2015).
44. C. D. Richardson, G. J. Ray, M. A. DeWitt, G. L. Curie, J. E. Corn, Enhancing homology-directed genome editing by catalytically active and inactive CRISPR-Cas9 using asymmetric donor DNA. *Nat. Biotechnol.* **34**, 339–344 (2016).
45. M. I. Love, W. Huber, S. Anders, Moderated estimation of fold change and dispersion for RNA-seq data with DESeq2. *Genome Biol.* **15**, 550 (2014).
46. M. J. Muraro, G. Dharmadhikari, D. Grun, N. Groen, T. Dielen, E. Jansen, L. van Gurp, M. A. Engelse, F. Carlotti, E. J. de Koning, A. van Oudenaarden, A single-cell transcriptome atlas of the human pancreas. *Cell Syst.* **3**, 385–394.e3 (2016).
47. S. C. van den Brink, F. Sage, A. Vertesy, B. Spanjaard, J. Peterson-Maduro, C. S. Baron, C. Robin, A. van Oudenaarden, Single-cell sequencing reveals dissociation-induced gene expression in tissue subpopulations. *Nat. Methods* **14**, 935–936 (2017).
48. T. Hashimshony, N. Senderovich, G. Avital, A. Klochendler, Y. de Leeuw, L. Anavy, D. Gennert, S. Li, K. J. Livak, O. Rozenblatt-Rosen, Y. Dor, A. Regev, I. Yanai, CEL-Seq2: Sensitive highly-multiplexed single-cell RNA-Seq. *Genome Biol.* **17**, 77 (2016).
49. S. Anders, W. Huber, Differential expression analysis for sequence count data. *Genome Biol.* **11**, R106 (2010).
50. D. Grun, L. Kester, A. van Oudenaarden, Validation of noise models for single-cell transcriptomics. *Nat. Methods* **11**, 637–640 (2014).

51. C. Trapnell, D. Cacchiarelli, J. Grimsby, P. Pokharel, S. Li, M. Morse, N. J. Lennon, K. J. Livak, T. S. Mikkelsen, J. L. Rinn, The dynamics and regulators of cell fate decisions are revealed by pseudotemporal ordering of single cells. *Nat. Biotechnol.* **32**, 381–386 (2014).
52. X. Qiu, Q. Mao, Y. Tang, L. Wang, R. Chawla, H. A. Pliner, C. Trapnell, Reversed graph embedding resolves complex single-cell trajectories. *Nat. Methods* **14**, 979–982 (2017).
53. S. A. Lambert, A. Jolma, L. F. Campitelli, P. K. Das, Y. Yin, M. Albu, X. Chen, J. Taipale, T. R. Hughes, M. T. Weirauch, The human transcription factors. *Cell* **172**, 650–665 (2018).

Acknowledgments: We thank H. V. Chen, J. C. Wu, M. Bellin, and C. Freund for providing the hiPSC lines and Y. Post for technical support. **Funding:** This work was supported by the Dutch CardioVascular Alliance (DCVA), an initiative with support of the Dutch Heart Foundation (DCVA2017-18 ARENA-PRIME to E.v.R. and 2015-30 eDETECT and 2018-30 PREDICT2 to J.P.v.T.). C.J.B. received funding from the European Union's Horizon 2020 research and innovation program under the Marie Skłodowska-Curie grant agreement no. 751988. **Author contributions:** A.K. and T.M. performed the hiPSC–cardiac cell and molecular biology experiments. S.J.v.K. performed the CRISPR-Cas9 targeting experiments. M.W., B.M., and C.J.B. performed the sequencing data analysis. J.M.-K. and I.P. maintained the hiPSC lines. A.M.S. and M.J.G. performed the primary human EPDCs experiments. J.P.v.T. supplied information on the prevalence of ACM pathogenic variants. A.K. and E.v.R. planned all experiments and wrote the manuscript. **Competing interests:** A.K. and E.v.R. filed a patent application #PCT/EP2020/051489 entitled "TFAP2 inhibition for treating cardiac disease involving fibro-fatty replacement." All other authors declare that they have no competing interests. **Data and materials availability:** All data associated with this study are present in the paper or the Supplementary Materials. Sequencing datasets generated in this study have been deposited in NCBI's Gene Expression Omnibus and are accessible through GEO Series accession number GSE152747.

Submitted 15 October 2020
Accepted 1 September 2021
Published 22 September 2021
10.1126/scitranslmed.abf2750

Citation: A. Kohela, S. J. van Kampen, T. Moens, M. Wehrens, B. Molenaar, C. J. Boogerd, J. Monshouwer-Kloots, I. Perini, M. J. Goumans, A. M. Smits, J. P. van Tintelen, E. van Rooij, Epicardial differentiation drives fibro-fatty remodeling in arrhythmogenic cardiomyopathy. *Sci. Transl. Med.* **13**, eabf2750 (2021).

Science Translational Medicine

Epicardial differentiation drives fibro-fatty remodeling in arrhythmogenic cardiomyopathy

Arwa KohelaSebastiaan J. van KampenTara MoensMartijn WehrensBas MolenaarCornelis J. BoogerdJantine Monshouwer-KlootsIlaria PeriniMarie José GoumansAnke M. SmitsJ. Peter van TintelenEva van Rooij

Sci. Transl. Med., 13 (612), eabf2750. • DOI: 10.1126/scitranslmed.abf2750

Understanding ACM

Arrhythmogenic cardiomyopathy (ACM) in humans is characterized by fibro-fatty deposits in the ventricles of the heart, but the mechanisms responsible for these deposits are not well understood, and current animal models of ACM do not recapitulate this phenotype well. Here, Kohela and colleagues generated human-induced pluripotent stem cells from patients with ACM, differentiated them into epicardial cells, and found that they spontaneously developed fibro-fatty cellular differentiation. Single-cell RNA sequencing analysis identified a transcription factor, TFAP2A, involved in the development of these deposits, and further analysis revealed that TFAP2A mediated epicardial differentiation by enhancing epithelial-to-mesenchymal transition. Although further studies are needed, these findings suggest that inhibition of TFAP2A might be a target for treating ACM.

Science Translational Medicine (ISSN) is published by the American Association for the Advancement of Science. 1200 New York Avenue NW, Washington, DC 20005. The title *Science Translational Medicine* is a registered trademark of AAAS.